Effect of the ageing on precipitation spatial distribution in stationary shoulder friction stir welded AA2050 alloys

Marie Noëlle Avettand Fenoël, F. de Geuser, A. Deschamps

Effect of the ageing on precipitation spatial distribution in stationary shoulder friction stir welded AA2050 alloys.

M.-N. Avettand-Fènoël[a,*], F. de Geuser[b], A. Deschamps[b]

[a]: Univ. Lille, CNRS, INRA, ENSCL, UMR 8207 - UMET - Unité Matériaux et Transformations, 59000 Lille, France
[b]: Université Grenoble Alpes, SIMAP, 38402 Saint Martin d'Hères, France

* Corresponding author – E-mail: marie-noelle.avettand-fenoel@univ-lille.fr
Tel: 33(0)320436927

Abstract

The spatial distribution of the strengthening precipitates in stationary shoulder friction stir welds (SSFSW) of the AA2050 Al-Cu-Li alloy has been characterized by small-angle X-ray scattering (SAXS), combined with micro-hardness mapping and transmission electron microscopy (TEM). It is shown that welding the alloy before ageing (T3WT8) leads to a more homogeneous distribution of precipitates along the weld zones than welding after ageing (T8W). Further in-situ SAXS ageing (24 h at 155°C) has been performed on the nuggets of both welds, to better evaluate the subsequent precipitate evolution. The nugget zone is shown to be very inhomogeneous, which can be explained by the 2 passes sequence of SSFSW. The mid-depth zone shows no fine precipitation, because of the formation of coarser phase consuming the solutes. Irrespective of the welding sequence, further ageing does not yield homogeneous precipitation in the welds.

Keywords

Stationary shoulder friction stir welding; AA2050 alloy; ageing; microstructure; SAXS analyses; microhardness

1. Introduction

Friction stir welding (FSW) which proceeds in the solid state, has been developed by the Welding Institute in 1991 **[1]** and is particularly suitable to join precipitation strengthened aluminum alloys **[2]**, among which AA2050 grade. This grade is an Al-Cu-Li alloy developed for its low density, high strength, high toughness and good corrosion resistance **[3]**. It can contain various precipitates such as θ' (Al_2Cu), δ' (Al_3Li), T_2 (Al_5Li_3Cu), T_B (Al_7Cu_4Li) and T_1 (Al_2CuLi) phase **[3]** which is known as the most effective strengthening precipitate in Al-Cu-Li alloys **[4-7]**. Few works dealing with thick AA2050 FSW joints are reported in literature and are focused on the investigation of material flow during welding **[8]**, on the joints corrosion resistance **[9-11]** and on their microstructure and mechanical properties **[3,12-17]**. However, the use of a rotational shoulder in conventional FSW was shown to result in a thermal gradient along the thick AA2050 joint depth entailing various precipitation states and then different mechanical properties as illustrated by the spatial distribution of hardness **[17]**.

A derivative of conventional FSW, called stationary shoulder friction stir welding (SSFSW), has been developed and consists in using a stationary shoulder, which slides over the surface of the workpiece, instead of a rotational shoulder **[18-19]**. With SSFSW process, almost no shoulder heat is generated hence resulting in a reduction of the temperature gradient between the top and bottom surfaces of the thick joint; consequently, nearly the whole energy

brought to the system results from the plastic work provided by the pin; the through-thickness weld profile is thus more parallel and uniform, the heat affected zone (HAZ) and the thermomechanical affected zone (TMAZ) are narrower compared to those obtained with conventional FSW **[20-22]** and the joint surface is smoother **[20,23]**. In addition, in terms of residual stresses, the tensile region is significantly narrower and the tensile residual stress magnitude is lower compared to conventional FSW **[21-22]**. A higher rotational speed **[21]** or a lower advancing speed **[24]** than in conventional FSW is however required in SSFSW in order to bring a suitable heat input to join the materials. SSFSW has already been used to weld aluminum alloys such as A6N01 **[25]**, AA2198-T851 **[23]**, AA2219-T6 **[26-27]**, AA6061-T6 **[28]**, 6005A-T6 **[29]**, AA6082 **[30]**, AA7010 **[21]**, AA7050-T7651 **[20,22,31]**, 7075-T651 **[24]** or even dissimilar Al alloys AA2024 / AA7050 **[32]**. A previous investigation was also devoted to SSFSW of AA2050 alloy and to the effect of a pre-treatment or post-welding treatment on joint microstructure and mechanical properties **[33]**. It evidenced the presence of B and $\overline{B}$ shear texture components in the probe affected zone of the nugget irrespective of the process sequence and, in a pre-treated sample, a slightly greater grain size across the nugget depth, a larger shoulder affected zone, the presence of Guinier Preston zones, a smaller microhardness undermatching and a lower uniform deformation **[33]**. The present paper aims to report a complementary investigation dealing with the characterization by Small Angle X-ray Scattering (SAXS) of the distribution of phases in terms of size and volume fraction, relying on the methodology developed and applied previously to conventional AA2050 friction-stir welds **[12,14,15]**. Microstructure maps will be realized along these thick AA2050 stationary shoulder friction-stir welds, and will be linked to microhardness maps. A further aim of this study is to analyze the effect of pre or post-weld ageing on these spatial distributions of precipitates and on the kinetics of precipitation during subsequent artificial ageing of the welds at 155°C. Finally, the pros and the cons of SSFSW in connection with the phases distributions will be discussed.

2. Experimental procedure

The base material is a AA2050 aluminum alloy whose chemical composition is reported in Table 1.

Table 1: Chemical composition range of the AA2050 alloy.

Element	Si	Fe	Cu	Mn	Mg	Zr	Li	Ag	Al
Mass.%	<0.08	<0.10	3.2 to 3.9	0.2 to 0.5	0.2 to 0.6	0.06 to 0.14	0.7 to 1.3	0.2 to 0.7	Balance

Two plates (15 mm thick, 200 mm wide and 400 mm long) were abutted and welded perpendicularly to the rolling direction either in a T3 state or in a T8 state (precipitation heat treated). Friction stir welding was conducted with a 0.5° backward-tilted tool made of MP159 (35.7% Co, 25.5% Ni, 19% Cr, 9% Fe, 7% Mo, 3% Ti, 0.6% Nb, 0.2%Al (mass.%)) material. The tool is constituted of a 21.5 mm diameter stationary shoulder prolonged by a pin. The 10 mm long pin was a left hand threaded truncated flute tool with a diameter of 10 mm at its root. The backing plate was made of XC48 steel. Welding was performed under a mean axial effort of 20-22 kN with a clockwise rotation speed of 400 rpm and at a welding speed of 100 mm/min. Two passes with air cooling down to room temperature in-between were carried out, one on each surface of the plate. The welding direction of the first and second passes were opposite so that the advancing side after the first pass corresponds to the advancing side after the second pass.

The T3 state was obtained according to the parameters defined in a patent **[34]**. The joint produced with the T3 material was then aged for a few tens of hours at a temperature close to 150°C and is referred to as the T3WT8 sample. The specimen aged in the aforementioned conditions before welding is referred to as the T8W sample.

The transverse sections of the joints were polished and etched for around 20 s with Keller's reagent (3 mL HNO_3, 6 mL HCl, 6 mL HF, 150 mL H_2O) in order to identify the various zones of the welds.

For transmission electron microscopy (TEM) / X-ray energy dispersive spectroscopy (EDX) analyses under a 200 kV accelerating voltage, thin foils were sampled in the nuggets generated by the second pass at different depths from the stirred top surface (4 and 8 mm). They were first mechanically polished down to a thickness of 50 µm. They were subsequently electropolished in a 25 vol.% nitric acid - 75 vol.% methanol solution at a temperature between -9 and -4°C with a voltage of 12.5 V and a current density in-between 18.1 and 22.6 A/cm². They were finally ion-milled with two 3 keV argon ion beams with a ±6° angle of incidence for 15 min.

For SAXS analyses, a slice was sampled in both joints along their transverse cross-sections. The slices were mechanically polished down to a thickness of 150 µm. SAXS was performed on a custom built laboratory setup with a rotating anode source at the K_α energy of Cu (about 8 keV). The sample-to-detector distance was about 0.6 m and the SAXS patterns were recorded by a PILATUS 2 300k hybrid pixel detector. To map the microstructure along the weld, the samples were scanned along 2 directions with a step size of 0.5 mm, recording 1421 images, spanning a total surface of 24 mm x 14 mm. Since the beam size was roughly 1 mm, it should be noted that the SAXS maps are slightly oversampled and details smaller than 1 mm are likely to be smoothed out.

For in situ experiments, a 4 mm vertical band along the nugget was cut from each sample. This band was then aged in situ for about 20 h at 155°C in a custom built furnace which allows scanning the sample while ageing. The temperature reached 155°C in less than a minute. We recorded a SAXS pattern every 1 mm at the centre of this band and repeated this scan for the duration of the in-situ experiments, resulting in a series of spatially resolved precipitation kinetics.

The interpretation of the SAXS signal was performed according to **[14]**. The precipitates are considered as flat cylinders. Their long dimension being too large with respect to the characteristics of the SAXS set-up, it cannot be evaluated from the data. Thus the results of the data fitting consist in the relative volume fraction of platelets as well as their thickness. T_1 and θ' can both be present and SAXS cannot distinguish between them. The results are thus to be interpreted as resulting from the combination of all platelets precipitates. The results are presented as 2D maps of size and volume fractions (in relative units). For the in-situ experiments, the maps axes are heat treatment time (X-axis) and position along the nugget height (Y-axis).

Vickers microhardness measurements were also carried out on the transverse cross sections of the welds under a 50 g load applied for 15 s. The microhardness measurements were performed every 200 µm along the X-axis and every 2 mm along the Y-axis. X-axis is along the weld height, Z-axis along the welding speed and Y-axis is defined such as the coordinate system (O, X, Y, Z) is direct (figure 1).

3. Results

3.1. Effect of the process sequence (T8W or T3WT8) on T_1/θ' 2D distribution.

Figure 1 displays the features of the transverse cross sections of the T3WT8 and T8W joints. Keller etching makes it possible to distinguish the different zones on both joints, namely the nugget, the thermomechanical affected zone (TMAZ), the heat affected zone (HAZ) whose microstructure differs from that of the base material. Given the pin length and its penetration depth, the nugget zone at workpiece mid-depth has been stirred twice by the pin during the 2 passes.

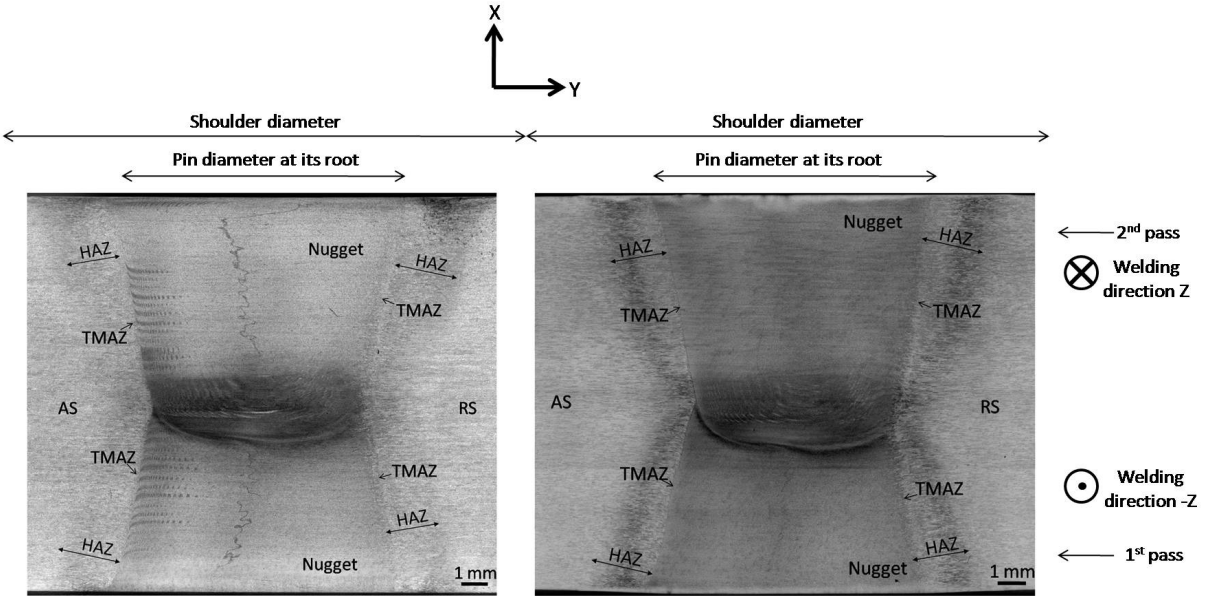

Figure 1: Transverse cross-sections (X-Y plane) of T3WT8 and T8W joints etched with Keller solutions (AS and RS are respective abbreviations for advancing and retreating side). It is worthy to note that the S-line in the nugget is less obvious in micrograph of T8W very likely because of differences of etching duration.

The 2D distribution of the volume fraction and thickness of T_1/θ' in both joints are respectively depicted in Figures 2 and 3. These maps clearly highlight the effect of welding on the precipitates distribution, particularly the drastic effect of the welding sequence.
In the sample aged after welding (T3WT8, Figure 2), there are precipitates in each zone of the weld, except at the centre of the nugget where no precipitates are detected. The rest of the nugget does not reach the precipitate fraction of the base material, with a smaller fraction by a factor of ~2. The HAZ area shows a very similar distribution of precipitates to that of the base material, confirming that the moderate heating experienced during welding has had no influence on the subsequent precipitation.

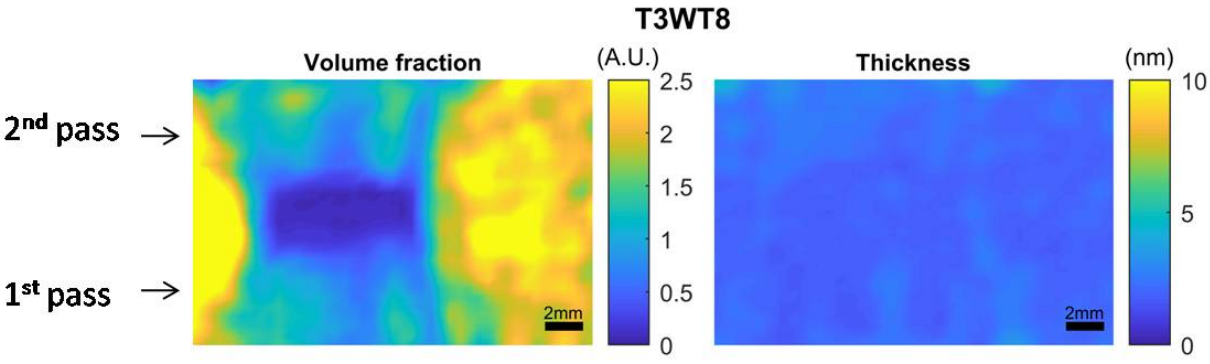

Figure 2: SAXS maps showing the 2D distribution of T_1/θ' in the X-Y plane for the T3WT8 sample. Compared to figure 1, the images in figure 2 are slightly shifted towards RS.

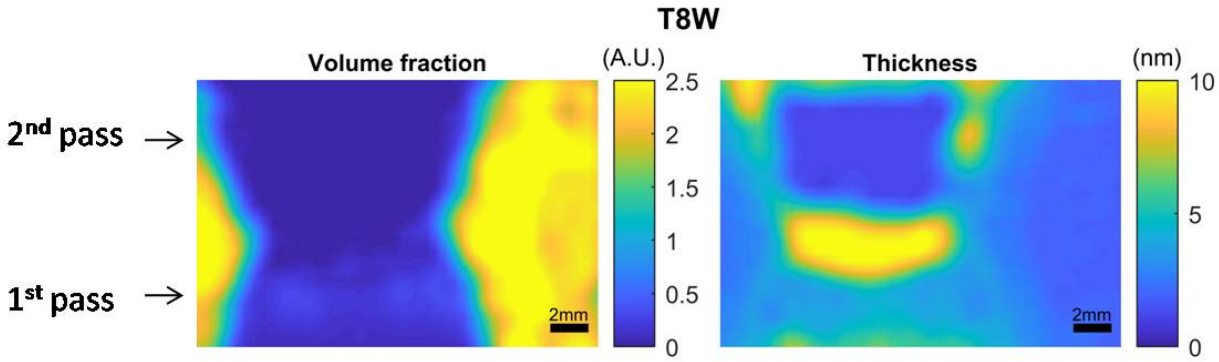

Figure 3: SAXS maps showing the 2D distribution of T_1/θ' in the X-Y plane for the T8W sample. Compared to figure 1, the images in figure 3 are slightly shifted towards RS.

In the sample welded after precipitation treatment (T8W, figure 3), the welding process has dissolved nearly all precipitates in the nugget. A low fraction of precipitates is detected in the area of the first pass, which can be attributed to the heat provided by the second pass. These precipitates are thicker than in the base material. The nugget bottom created by the second pass is shown to have much thicker precipitates than elsewhere, but with a negligible volume fraction, showing a strong coarsening in this area having undergone the 2 passes. These large sizes with negligible fractions are also observed at the borders of the nugget, mostly at the top part (second pass), suggesting strong coarsening of the precipitates when reaching a temperature just below their solvus.
In the HAZ area, the fraction of precipitates is slightly higher than in the base material, with a thickness relatively larger.

Figure 4 shows TEM observations within the weld. According to the observations of Figure 4 a and b, a mixture of T_1 and θ' is present in the center of the nugget of the T3WT8 sample generated by second pass.~~,~~ Figures 4a, b and c also depict the presence of T_1 phases on dislocations. B~~b~~ut no T_1 and θ' could be evidenced at the bottom of the~~is~~ nugget of T3WT8 (not shown here). Regarding the T8W sample, TEM analyses did not enable to detect T_1 and θ' phases neither in the centre of the nugget generated by the second pass (not shown here) nor at its bottom (figure 4~~c~~d). Besides, many Cu rich precipitates containing Fe, Mn or Mg and with a size close to 0.5 µm were identified at an 8 mm depth from the top surface in both joints (see example for T8W joint in figures 4~~d~~e to ~~i~~j). Other smaller Cu bearing particles without Fe, Mn and Mg were also observed at this location (see white arrows in figure 4g).

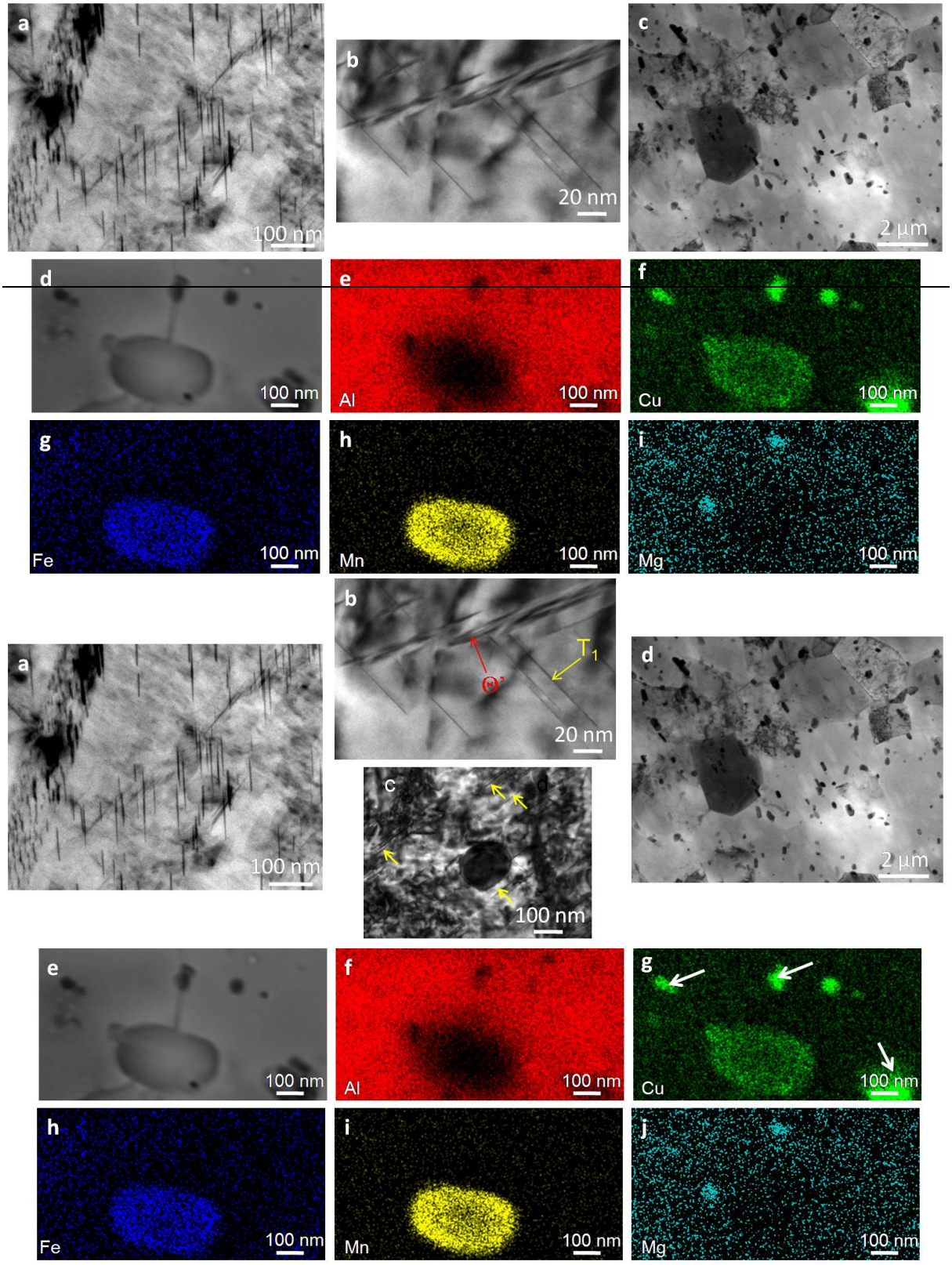

Figure 4: Examples of bright field transmission electron micrographs (close to <110>$_{Al}$) in the nugget central zone (X-Z plane) generated by the second pass at 4 mm from the stirred surface of T3WT8 joint (a, b, c), and at 8 mm from the stirred surface of T8W joint (~~e~~d). Details of figure ~~b~~d (~~d~~e) and linked X-ray maps of Al K$_\alpha$ (~~e~~f), Cu K$_\alpha$ (~~f~~g), Fe K$_\alpha$ (~~g~~h), Mn K$_\alpha$ (~~h~~i) and Mg K$_\alpha$ (~~i~~j).

3.2. Microhardness maps of joints T3WT8 and T8W.

Figure 5 shows microhardness maps of the section of the T3WT8 and T8W welds. It evidences that the softest zone in both joints is located in the nugget at the plate mid-thickness. This zone has experienced twice the effect of the pin and corresponds to the bottom of the nuggets generated by the two passes. Besides, in the remaining parts of the nugget, the microhardness of the nugget is greater in the T3WT8 sample than in the T8W specimen which is in agreement with the precipitates distribution obtained by SAXS.

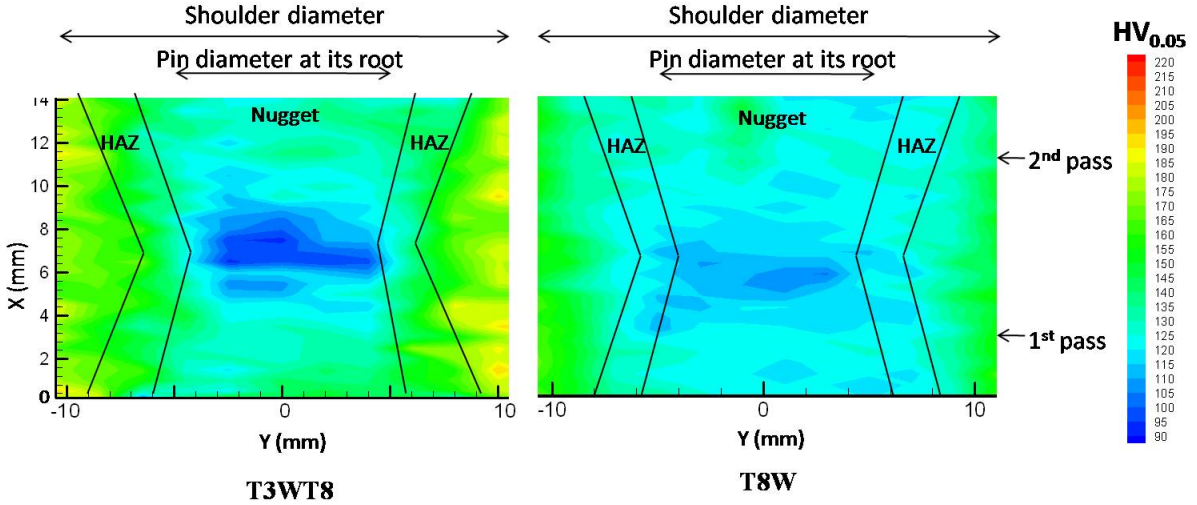

Figure 5: $HV_{0.05}$ microhardness maps of the transverse cross-sections (X-Y plane) of T3WT8 and T8W samples. The location of the faying interface corresponds to Y = 0 mm; the values on the X-axis are related to the distance from the stirred top surface during the first pass. The borders of the nugget and the HAZ are delineated in black and refer to their limits deduced from chemical etching in figure 1.

3.3. Effect of isothermal artificial ageing at 155°C on T_1 and θ' distribution in the nugget zone along the joints thickness.

From the in-situ SAXS experiments while heating the nugget zones, one can build time-dependent maps of the volume fraction of T_1 and θ' along the depth of the median part of the nugget in the welds transverse cross section (figure 6). For the T3WT8 joint (left figure), the results around position 0 show that precipitation of T_1 and θ' does not occur at nugget mid-depth even after an isothermal treatment at 155°C for 20 h. However, in the remaining part of the nugget of the same sample, the fraction of T_1 and θ' increases with holding time at 155°C which suggests that the material was still underaged after the initial T8 treatment. In the T8W weld, there is very little T_1 and θ' precipitation during isothermal ageing indicating a much slower kinetics. In both cases, the final state shows essentially no precipitates at mid-thickness.

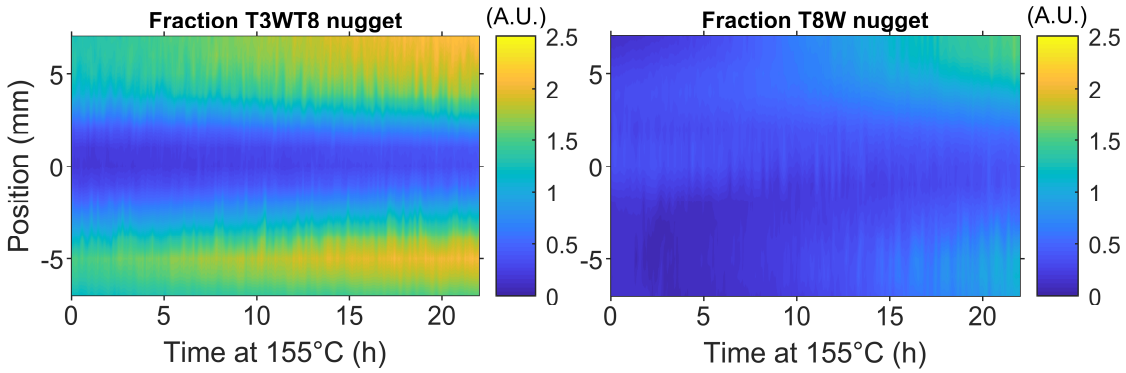

Figure 6: SAXS maps showing the evolution of the distribution of the volume fraction T_1 and θ' in the central zone of the nugget for both joints in the X-Y plane during isothermal treatment at 155°C. Position at 0 mm corresponds to the central nugget area mid-depth.

4. Discussion

4.1. Effect of pre- or post-ageing on the joint microstructure

According to SAXS (figure 3) and TEM analyses, no T_1 phase was observed in the central zone of the T8W joint formed during the second pass. It suggests that SSFSW leads to the dissolution of T_1 in the nugget. This observation is consistent with previous studies reported in literature on FSW joints of 2050 Al alloy in T8 state **[14]** or T3 state **[15]**. The combination of the homologous temperature (defined as the ratio between the absolute welding temperature and the absolute melting point of the material) reached in the nugget during FSW, at least of 0.6-0.7 **[35]**, which is usually in-between 400 and 550°C **[2,21,35-36]** in aluminum alloys, and of the strain, which is in the range [2- 130] in FSW **[37-42]**, is very likely suitable to dissolve the T_1 phase. Moreover, the temperature reached in the nugget during FSW is consistent with the temperature of dissolution of T_1 which is around 450°C according to DSC analyses performed with a heating rate of 10°C/min **[7,14,16]**. The heating rate during SSFSW is however greater than 10°C/min, which should increase the dissolution temperature of T_1 while the latter temperature may be decreased by the strain.

For the T3WT8, the post-welding heat treatment effectively triggers the precipitation of T_1 in the base material as expected. In the nugget, however, the precipitation treatment results in a much lower fraction of precipitates than in the base material. T_1 is known to preferentially nucleate at dislocations and subgrain boundaries **[5,7,43-46]**. Al-Cu-Li alloys are thus generally pre-stretched before ageing to accelerate the kinetics of T_1 precipitation, whose rate is monotonically increasing with the level of predeformation **[47-49]**. Since the dislocation density is much lower in the nugget than in the base material due to the high temperature reached and associated dynamic recrystallization, the amount of nucleation sites is lower, and thus the fraction of precipitates is lower. Some T_1 phases could indeed be observed on dislocations, whose density remains low (figure 4 a and c). It is also likely that the respective relative proportion of T_1 and θ' has changed, since the absence of dislocations has been shown to favour θ' compared to T_1 **[47]**. The proportion of T_1 and θ' phases has however not been estimated.

In both joints, SAXS analyses show the asymmetrical features of the nugget along the joint thickness (figures 2 and 3) which is generated by sequence of 2 passes.

The workpiece mid-depth is a very particular zone, since it can be considered as the thermomechanically affected zone (TMAZ) of both the 1st pass and the 2nd pass. This zone is characterized in both T3WT8 and T8W welds by the absence of T_1 and θ' according to SAXS analyses (figures 2 and 3) and TEM characterization (figure 4~~ed to ij~~). In this zone, coarse Cu

rich precipitates ~~sometimes~~ containing Mn, Fe or Mg together with smaller Cu bearing ones which are Mn, Fe or Mg free (see white arrows in figure 4g) are detected ~~have been formed~~ (figure ~~4d~~e to ~~i~~j). The smaller Cu bearing precipitates ~~and~~ have very likely consumed the Cu solute required to form T_1 and θ'. Concerning the coarser precipitates, the same kinds of Mn, Fe or Mg rich precipitates have already been detected in the case of FSW of 2050 alloy **[15]**. Given their size, ~~T~~these large precipitates are very likely native particles of the base material, which were not dissolved during SSFSW.~~, which were formed either during welding or during the cooling stage after welding,~~ They are thermally stable at processing temperature and do not seem to be affected by strain. Below the pin, the material downflow is blocked by the cold die effect **[8]** of the mid-thickness of AA2050 thick workpiece which presents a low thermal conductivity of 76.6 W/m/K (at 20°C) in T3 state compared to that of many aluminum alloys **[50]**. It plays the role of a backing plate and induces some vortices and a subsequent material upflow leading to the formation of onion half cups in the nugget **[8]**. The thermal diffusivity of AA2050 alloy in T3 state close to 3.15 10^{-5} m²/s, which is intermediate between that of Al of 9.7 10^{-5} m²/s and that of steel of 1.2-1.5 10^{-5} m²/s, suggests that at the nugget root, the temperature is colder than at the stirred surface. Another study about FSW of 25 mm thick AA 6061 alloy has already proved the importance of the nature of the material playing the role of the backing plate on the temperature evolution along the joint depth **[51]**. The assumption according to which the temperature is reduced along the SSFSW depth during welding is also consistent with thermal modeling results performed in the case of SSFSW of 6.5 mm thick AA7050-T7651 **[20]**. Finally, this hypothesis of temperature reduction along the SSFSW joint depth seems to be realistic since the grain size near the stirred surface was shown to be greater than at the plate mid-depth **[33]**. The lower temperature at nugget root during a pass, together with a possible lower cooling rate could thus explain why phases other than T_1 and θ' ~~were formed~~ are detected at joint mid-depth.

In the T8W joint, the T_1 and θ' precipitates have coarsened and their fraction has increased in the HAZ, indicating that the material was still in an underaged condition, which is consistent with previous studies **[48,52]** which have shown that these types of alloys undergo additional precipitation, and especially an increase in thickness, when aged at a temperature above their T8 ageing temperature. These results are also consistent with other FSW studies reported in the literature **[7,16]**. In the nugget, while it seems clear that the heat and strain due to the SSFSW have dissolved most of the T_1 and θ' precipitates (figure 3), the 2^{nd} pass seems to have affected the 1^{st} pass zone of the nugget, since some precipitates are present. This suggests that the 1^{st} pass area has been affected by the heat input of the second pass.

In T3WT8 specimen, the volume fraction of T_1 and θ' is more symmetrical from either side of the joint mid-depth (figure 2). The volume fraction of these phases is however more important in the 1^{st} pass part of the nugget and closer to the stirred surface, because of the heat received during the 2^{nd} pass, which may have initiated the nucleation of T_1 and θ', before their further development during T8 post-weld ageing. It is worth noting that, contrarily to T8W, no coarsening of T_1 and θ' is observed in the HAZ of T3WT8 sample (figure 3). This can be explained by the sequence of treatments. Since the precipitates were formed after the welding process, they were not affected by the additional heat during the weld, whereas in the T8W process, the precipitates in the HAZ were already present when it was heat-affected.

To summarize, the post-weld ageing leads to a more homogeneous microstructure along the weld depth except at mid-depth.

According to Hall-Petch relationship, the hardening due to a reduction of the grain size is expected to be significant for aluminum alloys **[53]**. Nevertheless, according to a previous paper dealing with the current joints **[33]**, the mean grain size in the nuggets generated by the second pass is rather similar for both joints; actually it evolves from 14.3 (11.9) µm just

below the stirred surface to 4.8 (2.9) µm at the nugget bottom for the T8W and T3WT8 samples respectively; the widths of the grains distribution are also roughly similar for both samples **[33]**; thus the marked differences of hardening between T3W and T3WT8 joints cannot be explained by the very slight differences of grain size, but rather by the different states of precipitation. Actually, the T_1 phase is known as the most effective strengthening phase in Al-Cu-Li alloy **[4-7]** among which AA2050 alloy **[3]**. And figures 2, 3 and 5 obviously show that ~~T~~the distribution maps of the volume fraction of T_1 and θ' along the weld depth ~~(figures 2 and 3)~~ are consistent with the hardness maps of the transverse section of the joints ~~in figure 5~~; the absence of T_1 at joint mid-depth in the nugget is linked to a marked softening. The stationary shoulder which is generally used to reduce the thermal gradient along the plate thickness **[18-19]** does not enable to homogenize the microstructure and the hardness. Indeed, the present case is concerned by SSFSW of an age hardenable alloy whose precipitation state is sensitive to the different temperatures, local strains and strain rates experienced along the plate thickness during welding. This result has already been faced in terms of grain size and microstructure along the joint depth in the case of SSFSW of AA2050 **[33]**, of AA7050 **[20]** or of AA7010 **[21]**. These observations can very likely be explained by the use of a slightly conical Triflat pin shape which entails more heat at the stirred surface and by the cold die effect of the mid-thick AA2050 workpiece (which plays the role of backing plate since, in the present case, welding is performed on mid-thickness), which leads to heat loss at the weld root. Another explanation could be also related to the decreasing dislocations densities along the joint depth from the weld top to the nugget root, even if they are low. These dislocations could have been introduced in the nugget by the internal stresses entailed during the cooling stage of welding, in greater amounts at the weld top since the higher temperature peak during welding entails a higher cooling rate at this location.

4.2. Kinetics of precipitation in the nugget during artificial ageing at 155°C

During artificial ageing, no precipitation was observed by SAXS in the nugget central zone (at plate mid-thickness) in both samples (figure 6). As previously discussed, a large part of the solute must have been trapped during SSFSW to form ~~coarse~~ Cu rich precipitates ~~sometimes containing Mn, Fe or Mg~~ (figure 4~~c~~d to ~~i~~j) and was not available any more to lead to the precipitation of T_1 and θ' during artificial ageing.

In the remaining parts of the nugget, T_1 and θ' precipitation kinetics is slower in T8W compared to T3WT8 during artificial ageing (figure 6), which is consistent with DSC results related to T_1 precipitation and obtained with a heating rate of 10°C/min **[33]**. Indeed, in the remaining parts of the nugget in T8W, neither natural ageing nor artificial aging up to 18 h at 155°C leads to significant T_1 and θ' precipitation. These results can be explained by the longer duration of ageing in the case of T3WT8 due to the addition of the T8 treatment and further in-situ aging at 155°C. The T8 treatment thus permitted a preliminary precipitation to occur in the T3WT8 nugget, which further develops during artificial ageing at 155°C. This observation highlights the fact that T_1 precipitation, which is known to occur at temperatures between ~100 to ~350°C according to a time-temperature-precipitation diagram of an alloy similar to AA2050 **[~~53~~54]**, occurs with a very slow kinetics at 155°C in the absence, or very low, density of dislocations **[15, ~~54~~55]**, which are the preferential nucleation sites for this phase **[5]**. In the weld nugget, the low dislocations density can be explained by dynamic recrystallization occurring during welding.

Moreover, the precipitate distribution of T_1 and θ' is heterogeneous along the nugget depth (figure 6). The fraction of precipitates reached at the end of the investigated heat treatment increases with the distance to the nugget centre. This observation confirms the DSC results obtained with a heating rate of 10°C/min on the T3WT8 joint sampled at different depths in the nugget get by the second pass **[33]**. It suggests that there are more nucleation

sites of T_1 at the top surface than at joint mid-depth before artificial ageing. It seems to confirm once again and as previously explained, that, before artificial ageing, the temperature during SSFSW decreased from the stirred surfaces towards the joint mid-depth. The temperature reduction along the joint depth is all the more important that the plate is thick and that welding was performed on mid-thickness. As aforesaid, the big grains near the stirred surface very likely contain slightly more dislocations entailed by internal stresses during welding cooling stage than those at plate mid-depth, because of higher cooling rate. Near the stirred surface, the greater heat input during welding and the higher density of dislocations introduced during cooling stage of welding have very likely contributed to the formation of more T_1 nucleation sites and could thus explain the faster kinetics of T_1 precipitation. Previous studies on similar alloys such as AA2198 or AF/C 458 alloy have already shown that increasing stretch levels result in increasing T_1 precipitate density **[5,47-49]** and smaller T_1 size **[47-48]**. The in-situ SAXS experiment for a 20 h holding time thus enables to highlight the heterogeneity of the microstructure in the nugget of T3WT8.

For both joints, the additional ageing treatment at 155°C for 20 h is insufficient to reach the base material microstructure because of the various precipitation states developed in the nuggets following the different thermomechanical histories they experienced during FSW.

It is finally worth noting that the T_1 and θ' volume fraction map of the T8W nugget central area after 20 h of artificial ageing at 155°C corresponds to that of T3WT8 nugget central part. This observation suggests that T8 treatment corresponds to an artificial ageing of about 20 h at 155°C. The material in the T8 state does not seem to be more difficult to weld than in the T3 state, although the AA2050 in the T8 state is harder than in the T3 state at room temperature. Indeed, to be welded, the material must reach a homologous temperature of 0.6-0.7, as mentioned above. At this temperature, the dissolution of the T_1 strengthening phase occurs in both T3 and T8 state and the material to be welded is soft. The constitutive laws of AA2050 in T3 and T8 state are very likely similar at the welding temperature.

5. Conclusions

SAXS analyses have evidenced the asymmetry of precipitation along the 15 mm depth of the nuggets generated by the 2 SSFSW passes. This is true for both sequences of processing (T3WT8 and T8W). Because of the 2 passes, the central zone of the nugget experienced different thermomechanical histories along its depth. In fact, the tool movement during the second pass generated some additional strain under the pin as well as extra heat input in the nugget resulting from the 1st pass leading to a change of its precipitation state. In addition, even after artificial ageing at 155°C for 20 h and whatever the joint, no precipitation of T_1 and θ' phases occurred at the soft mid-depth of the nugget zone which experienced the FSW tool movement twice, very likely because of the formation of other Cu-rich precipitates in this zone which trapped the solute required for the precipitation of T_1 and θ'.

Although friction stir welding was performed with a stationary shoulder to join a 15 mm thick plate, it did not give rise to a homogenization of the microstructure along the thickness of joint. This microstructural heterogeneity indeed directly results from the precipitation states linked to the thermomechanical history generated during welding.

Aknowledgements

The authors are very thankful to Constellium C-TEC Voreppe Research Centre, France for providing the joints.

Data availability

All the data in this manuscript are available upon request to the corresponding author.

References

[1] W.M. Thomas, E.D. Nicholas, J.C. Needham, M.G. Murch, P. Temple-Smith, C.J. Dawes, Improvements relating to friction welding (1991) GB patent n° 9125978-8

[2] P. Threadgill, A. Leonard, H. Shercliff, P. Withers, Friction stir welding of aluminum alloys, Int. Mater. Rev. 54 (2009) 49-93.

[3] P. Lequeu, K.P. Smith, A. Daniélou, Aluminum-copper-lithium alloy 2050 developed for medium to thick plate, J. Mater. Eng. Perf. 19 (2010) 841-847.

[4] J.C. Huang, A.J. Ardell, Addition rules and the contribution of δ' precipitates to strengthening of aged Al-Li-Cu alloys, Acta Metall., 36 (1988) 2995-3006.

[5] W.A. Cassada, G.J. Shiflet, E.A. Starke, The effect of plastic deformation on T_1 precipitation, J. Physique C3, supplement au n°9, 48 (1987) 397-406.

[6] B. Decreus, A. Deschamps, F. De Geuser, P. Donnadieu, C. Sigli, M. Weyland, The influence of Cu/Li ratio on precipitation in Al-Cu-Li-x alloys, Acta Mater. 61 (2013) 2207-2218.

[7] H. Sidhar, R.S. Mishra, Aging kinetics of friction stir welded Al-Cu-Li-Mg-Ag and Al-Cu-Li-Mg alloys, Mater. Design 110 (2016) 60-71.

[8] M.-N. Avettand-Fènoël, R. Taillard, J. Laye, T. Odièvre, Experimental investigation of three-dimensional (3-D) material flow pattern in thick dissimilar 2050 friciton stir welds, Met. Mat. Trans. A 45(2) (2014) 563-578.

[9] V. Proton, J. Alexis, E. Andrieu, C. Blanc, J. Delfosse, L. Lacroix, G. Odemer, Influence of post-welding heat treament on the corrosion behavior of a 2050-T3 aluminum-copper-lithium alloy friction stir welding joint, J. Electrochem. Soc. 158(5) (2011) C139-C147.

[10] V. Proton, J. Alexis, E. Andrieu, J. Delfosse, M.-C. Lafont, C. Blanc, Characterisation and understanding of the corrosion behaviour of the nugget in a 2050 aluminium alloy friction stir welding, Corrosion Sci. 73 (2013) 130-142.

[11] M. Dhondt, I. Aubert, N. Saintier, J.M. Olive, Effects of microstructure and local mechanical fields on intergranular stress corrosion cracking of a friction stir welded aluminum-copper-lithium 2050 nugget, Corrosion Sci. 86 (2014) 123-130.

[12] F. De Geuser, F. Bley, A. Denquin, A. Deschamps, Mapping the mcirostructure of a friction stir welded (FSW) Al-Li-Cu alloy, J. Physics : Conference Series 247 (2010) 012034.

[13] M. Dhondt, I. Aubert, N. Saintier, J.M. Olive, Mechnaical behavior of periodical microstructure induced by friction stir welding on Al-Cu-Li 2050 alloy, Mater. Sci. Engin. A 644 (2015) 69-75.

[14] F. De Geuser, B. Malard, A. Deschamps, Microstructure mapping of a friction stir welded AA2050 Al-Li-Cu in the T8 state, Phil. Mag. 94 (2014) 1451-1462.

[15] B. Malard, F. De Geuser, A. Deschamps, Microstructure distribution in an AA2050 T34 friction stir welds and its evolution during post-welding heat treatment, Acta Mater. 101 (2015) 90-100.

[16] H. Sidhar, R.S. Mishra, A.P. Reynolds, J.A. Baumann, Impact of thermal management on post weld heat treatment efficacy in friction stir welded 2050-T3 alloy, J. Alloys Compnds. 722 (2017) 330-338.

[17] M.-N. Avettand-Fènoël, R. Taillard, Heterogeneity of the nugget microstructure in a thick 2050 Al friction stir weld, Met. Mater. Trans. A 46(1) (2015) 300-314.

[18] C.A. Widener, J.E. Talia, B.M. Tweedy, D.A. Burford, High rotational speed friction stir welding with a fixed shoulder, 6th international friction stir welding symposium (2006)

[19] M.J. Russell, M.E. Nunn, J. Martin, Recent developments in the stationary shoulder FSW of titatnium alloys. In: proceedings of 7th International symposium on friction stir welding, TWI, Japan (2008)

[20] H. Wu, Y.C. Chen, D. Strong, P. Prangnell, Stationary shoulder FSW for joining high strength aluminum alloys, J. Mater. Process. Technol. 221 (2015) 187-196.

[21] T. Sun, M.J. Roy, D. Strong, P.J. Withers, P.B. Prangnell, Comparison of residual stress distributions in conventional and stationary shoulder high-strength aluminum alloy friction stir welds, J. Mater. Process. Technol. 242 (2017) 92-100.

[22] T. Sun, A.P. Reynolds, M.J. Roy, P.J. Withers, P.B. Prangnell, The effect of shoulder coupling on the residual stress and hardness distribution in AA7050 friction stir butt welds, Mater. Sci. Engin. A 735 (2018) 218-227.

[23] J. Goebel, M. Reimann, A. Norman, J.F. Dos Santos, Semi-stationary shoulder bobbin tool friction stir welding of AA2198-T851, J. Mater. Process. Technol., 245 (2017) 37-45.

[24] D. Li, X. Yang, L. Cui, F. He, X. Zhang, Investigation of stationary shoulder friction stir welding of aluminum alloy 7075-T651, J. Mater. Process. Technol. 222 (2015) 391-398.

[25] T. Suda, Y. Sakamoto, T. Miyamichi, T. Sato, A feasibility study for stationary shoulder self-reacting pin tool welding, 9th symposium on friction stir welding, 2012, Huntsville

[26] J.Q. Li, H.J. Liu, Effects of tool rotation speed on microstructures and mechanical properties of AA2219-T6 welded by the external non-rotational shoulder assisted friction stir welding, Mater. Design 43 (2013) 299-306.

[27] H. Liu, Y. Hu, H. Wang, S. Du, D.P. Sekulic, Stationary shoulder supporting and tilting pin penetrating friction stir welding, J. Mater. Process. Technol. 255 (2018) 596-604.

[28] D. Li, X. Yang, L. Cui, F. He, H. Shen, Effect of welding parameters on microstructure and mechanical properties of AA6061-T6 butt welded joints by stationary shoulder friction stir welding, Mater. Design 64 (2014) 251-260.

[29] S.D. Ji, X.C. Meng, J.G. Liu, L.G. Zhang, S.S. Gao, Formation and mechanical properties of stationary shoulder friction stir welded 6005A-T6 aluminum alloy, Mater. Design, 62 (2014) 113-117.

[30] M.M.Z. Ahmed, B.P. Wynne, W.M. Rainforth, P.L. Threadgill, Through-thickness crystallographic texture of stationary shoulder friction stir welded aluminium, Scripta Mater. 64 (2011) 45-48.

[31] T. Sun, M.J. Roy, D. Strong, C. Simpson, P.J. Withers, P.B. Prangnell, Weld zone and residual stress development in AA7050 stationary shoulder friction stir T-joint weld, J. Mater. Process. Technol. 263 (2019) 256-265.

[32] A. Barbini, J. Carstensen, J.F. Dos Santos, Influence of non-rotating shoulder on heat generation, microstructure and mechanical properties of dissimilar AA2024/AA7050 FSW joints, J. Mater. Sci. Technol. 34 (2018) 119-127.

[33] M.-N. Avettand-Fènoël, R. Taillard, Effect of a pre or postweld heat treatment on microstructure and mechanical properties of an AA2050 weld obtained by SSFSW, Mater. Design 89 (2016) 348-361.

[34] I. Bordesoules, A. Daniélou, C. Hénon, P. Lequeu, Method for assembling parts made of an aluminum alloy by welding, compressing sold deformation followed by the post-welding tempering of the entire welded area, International patent WO2010/130887 A1, November 2010

[35] R.S. Mishra, Z.Y. Ma, Friction stir welding and processing, Mater. Sci. Engin. R, 50 (2005) 1–78.

[36] R.S. Mishra, M.W. Mahoney, Friction stir welding and processing, ASM International 2007

[37] K. Masaki, Y.S. Sato, M. Maeda, H. Kokawa, Experimental simulation of recrystallized microstructure in friction stir welded Al alloy using a plane-strain compression test, Scripta Mater. 58 (2008) 355–360.

[38] A. Arora, Z. Zhang, A. De, T. DebRoy, Strains and strain rates during friction stir welding, Scripta Mater., 61 (2009) 863–866.

[39] G. Buffa, J. Hua, R. Shivpuri, L. Fratini, Design of the friction stir welding tool using the continuum based FEM model, Mater. Sci. Engin. A 419 (2006) 381–388.

[40] P. Heurtier, C. Desrayaud, F. Montheillet, A thermomechanical analysis of the friction stir welding process, Mater. Sci. Forum 396-402 (2002) 1537–42.

[41] H. Schmidt, J. Hattel, A local model for the thermomechanical conditions in friction stir welding, Mater. Sci. Engin. A, 13 (2005) 77–93.

[42] G. Buffa, J. Hua, R. Shivpuri, L. Fratini, A continuum based fem model for friction stir welding—model development, Mater. Sci. Engin. A 419 (2006) 389–396.

[43] W.A. Cassada, G.J. Shiflet, E.A. Starke, Mechanism of Al_2CuLi (T_1) nucleation and growth, Met. Mater.Trans. A 22 (1991) 287-297.

[44] W.A. Cassada, G.J. Shiflet, E.A. Starke, The effect of plastic deformation on Al_2CuLi (T_1) precipitation, Met. Mater. Trans. A 22 (1991) 299-306.

[45] K.S. Kumar, S.A. Brown, J.R. Pickens, Microstructural evolution during aging of an Al-Cu-Li-Ag-Mg-Zr alloy, Acta Mater. 44(5) (1996) 1899-1915.

[46] Y. Li, Z. Shi, J. Lin, Y.L. Yang, B.M. Huang, T.F. Ching, J.R. Yang, Experimental investigation of tension and compression creep-ageing behavior of AA2050 with different initial tempers, Mater. Sci. Engin. A 657 (2016) 299-308.

[47] B.M. Gable, A.W. Zhu, A.A. Csontos, E.A. Starke, The role of plastic deformation on the competitive microstructural evolution and mechanical properties of a novel Al-Li-Cu-X alloy, J. Light Met. 1 (2001) 1-14.

[48] T. Dorin, A. Deschamps, F. De Geuser, C. Sigli, Quantification and modelling of the microstructure/strength relationship by tailoring the morphological parameters of the T1 phase in an Al–Cu–Li alloy, Acta Mater. 75 (2014) 134-146.

[49] T. Dorin, A. Deschamps, F. De Geuser, F. Robaut, Impact of grain microstructure on the heterogeneity of precipitation strengthening in an Al-Li-Cu alloy, Mater. Sci. Engin. A 627 (2015) 51-55.

[50] E.A. Brandes, G.B. Brook, Smithells Metals Reference Book, Butterworth Heinemann, Oxford, 1992.

[51] P. Upadhyay, A. Reynolds, Effect of backing plate thermal property on friciton stir welding of 25 mm thick AA6061, Met. Mat. Trans. 45 (2014) 2091.

[52] T. Dorin, A. Deschamps, F. de Geuser, W. Lefebvre, C. Sigli, Quantitative description of the T1 formation kinetics in an Al-Cu-Li alloy using differential scanning calorimetry, small angle X-ray scattering and transmission electron microscopy, Phil. Mag. 94(10) (2014) 1012-1030.

[53] A. Kelly and R.B. Nicholson, eds.: Strengthening Methods in Crystals, Elsevier Materials Science Series, Great Yarmouth, Norfolk, England, 1971

[~~53~~54] J.A. Schneider, A.C. Nunes, P.S. Chen, G. Steele, TEM study of the FSW nugget in AA2195-T81, J. Mater. Sci. 40 (2005) 4341-4345.

[~~54~~55] B. Decreus, A. Deschamps, F. De Geuser, C. Sigli, Influence of natural ageing & deformation on precipitation in an Al-Cu-Li alloy, Adv. Eng. Mat. 15(11) (2013) 1082-1085.